ACS APPLIED MATERIALS & INTERFACES

Research Article

Cite This: ACS Appl. Mater. Interfaces 2018, 10, 44494−44500

www.acsami.org

Epitaxial Thin Films as a Model System for Li-Ion Conductivity in $Li_4Ti_5O_{12}$

Francesco Pagani,[‡,§] Evelyn Stilp,[‡] Reto Pfenninger,[§,∥] Eduardo Cuervo Reyes,[‡,†] Arndt Remhof,[‡] Zoltan Balogh-Michels,[‡] Antonia Neels,[‡] Jordi Sastre-Pellicer,[‡] Michael Stiefel,[‡] Max Döbeli,[#] Marta D. Rossell,[‡] Rolf Erni,[‡] Jennifer L. M. Rupp,[§,∥,⊥] and Corsin Battaglia[*,‡]

[‡]Empa, Swiss Federal Laboratories for Materials Science and Technology, 8600 Dübendorf, Switzerland

[§]Electrochemical Materials and [#]Ion Beam Physics, ETH Zürich, 8093 Zürich, Switzerland

[∥]Electrochemical Materials, Department of Materials Science and Engineering and [⊥]Electrochemical Materials, Department of Electrical Engineering and Computer Science, Massachusetts Institute of Technology, Cambridge, Massachusetts 02139, United States

Supporting Information

ABSTRACT: Using an epitaxial thin-film model system deposited by pulsed laser deposition (PLD), we study the Li-ion conductivity in $Li_4Ti_5O_{12}$, a common anode material for Li-ion batteries. Epitaxy, phase purity, and film composition across the film thickness are verified employing out-of-plane and in-plane X-ray diffraction, transmission electron microscopy, time-of-flight mass spectrometry, and elastic recoil detection analysis. We find that epitaxial $Li_4Ti_5O_{12}$ behaves like an ideal ionic conductor that is well described by a parallel RC equivalent circuit, with an ionic conductivity of 2.5×10^{-5} S/cm at 230 °C and an activation energy of 0.79 eV in the measured temperature range of 205 to 350 °C. Differently, in a co-deposited polycrystalline $Li_4Ti_5O_{12}$ thin film with an average in-plane grain size of <10 nm, a more complex behavior with contributions from two distinct processes is observed. Ultimately, epitaxial $Li_4Ti_5O_{12}$ thin films can be grown by PLD and reveal suitable transport properties for further implementation as zero-strain and grain boundary free anodes in future solid-state microbattery designs.

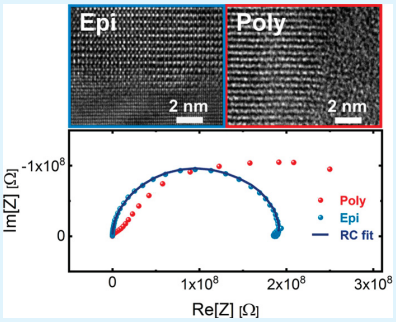

KEYWORDS: *$Li_4Ti_5O_{12}$, LTO, epitaxial, polycrystalline, thin film, anode, battery, pulsed laser deposition*

INTRODUCTION

$Li_4Ti_5O_{12}$ has generated significant interest because of its high cycling stability (zero-strain material) and high rate capability during lithium intercalation leading to its commercialization as an anode in Li-ion batteries.[1−3] As a result of these properties, $Li_4Ti_5O_{12}$ is also a promising anode material for all-solid-state batteries and thin-film microbatteries.[4−6] In a commercial Li-ion battery, the porous composite electrodes are infiltrated with liquid electrolyte and contain typically the active material, the conductive carbonaceous additives, and the binder, making it difficult to isolate fundamental materials transport properties. Conversely, thin films of a single active material can act as ideal model systems; for example, $Li_4Ti_5O_{12}$ thin films have been used to study phase transformations upon Li-ion insertion,[7] surface reactions with the organic electrolyte,[8,9] and the relationship between nanoscale structure and rate capability.[2] Moreover, $Li_4Ti_5O_{12}$ thin films were recently demonstrated to be promising candidates for all-solid-state batteries.[10] Surprisingly, there are no studies yet investigating the Li-ion conductivity and the role of grain boundaries in $Li_4Ti_5O_{12}$ thin films. The Li-ion conductivity of $Li_4Ti_5O_{12}$ has been examined on pressed and sintered pellets;[11−13] however, reported values in the literature vary substantially, possibly because of variations in grain size, lithium content, and other factors.

Here, we prepared epitaxial, single-crystal, and strain-free thin films as model systems to extract the Li-ion conductivity of $Li_4Ti_5O_{12}$ and compare them to polycrystalline films, representing a nonideal system, including grain boundaries. Using electrochemical impedance spectroscopy (EIS), we show that the epitaxial film behaves like an ideal Li-ion conductor with a (frequency independent) conductivity of 2.5×10^{-5} S/cm at 230 °C and an activation energy of 0.79 eV, whereas the polycrystalline film shows a more complex behavior that hints at ion trapping at the grain boundaries, which precludes the extraction of the ionic conductivity. These results demonstrate the importance of using epitaxial thin films to study Li-ion conductivity in $Li_4Ti_5O_{12}$ and show that epitaxial $Li_4Ti_5O_{12}$ thin films are promising anodes for their integration in microbatteries due to the absence of grain boundaries.

Received: September 21, 2018
Accepted: November 29, 2018
Published: November 29, 2018

Downloaded by MASSACHUSETTS INST OF TECHNOLOGY at 07:41:43:865 on June 18, 2019
from https://pubs.acs.org/doi/10.1021/acsami.8b16519.

ACS Publications © 2018 American Chemical Society

SEL 2010
Amperex v. SEL
IPR2023-01349

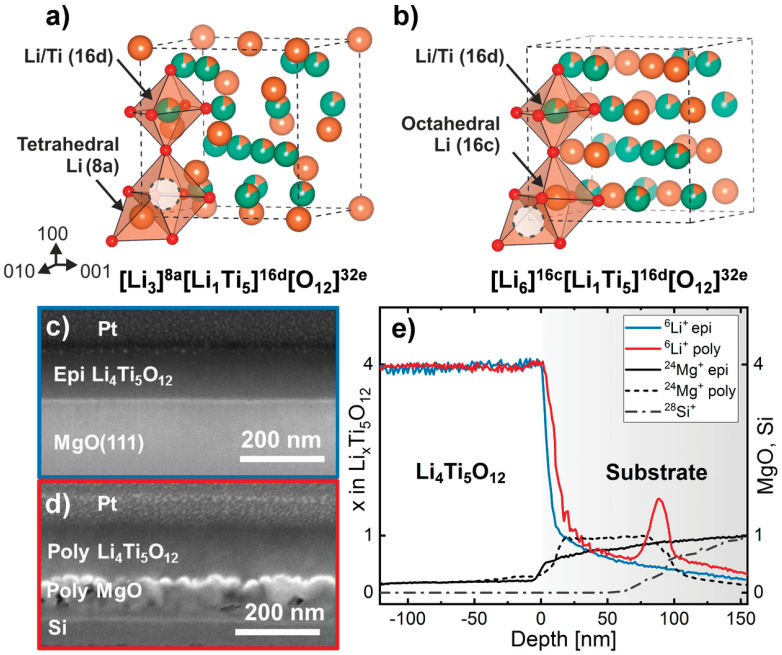

Figure 1. Crystal structure of (a) spinel $Li_4Ti_5O_{12}$ and (b) rock-salt $Li_7Ti_5O_{12}$. Orange, green, and red spheres represent lithium, titanium, and oxygen atoms, respectively, and the dashed circle represents the empty site. The 16d sites are occupied by titanium or lithium with occupancy ratio 5:1. (c,d) FIB cross section of (c) epitaxial and (d) polycrystalline $Li_4Ti_5O_{12}$ imaged by SEM. (e) $^6Li^+$ profile of epitaxial and polycrystalline $Li_4Ti_5O_{12}$ films by TOF-SIMS calibrated with ERDA. Black and gray lines represent Mg^+ and Si^+ signals, respectively.

EXPERIMENTAL

$Li_4Ti_5O_{12}$ thin films were deposited by pulsed laser deposition (PLD) at a substrate temperature of 500 °C in an oxygen atmosphere at a pressure of 13 mTorr and a substrate−target distance of 70 mm, employing a KrF excimer laser (wavelength 248 nm). The laser fluence was set to 2.6 J/cm^2, and the frequency was set to 10 Hz. The epitaxial $Li_4Ti_5O_{12}$ film was deposited on a MgO(111) single-crystal substrate (CrysTec), and the polycrystalline $Li_4Ti_5O_{12}$ film was deposited on a sputtered polycrystalline MgO film on Si(100) (University Wafer, ρ = 1−10 Ω cm). The target for PLD was prepared by mixing and grinding Li_2CO_3 (Sigma-Aldrich, 99%) and TiO_2 rutile (Sigma-Aldrich, 99.995%) to get an overlithiated target with a composition of $Li_{5.35}Ti_5O_{12}$. The mixed powder was calcined at 850 °C for 12 h, uniaxially and subsequently isostatically pressed, and finally sintered at 1000 °C for 12 h (heating rate of 10 °C/min) under a constant flow of 30 sccm O_2.

Scanning electron microscopy (SEM) images were acquired on a FEI Helios NanoLab 660 using an accelerating voltage of 5 kV. Focused-ion-beam (FIB) cuts were performed on the same tool using a Ga^+ ion beam at an accelerating voltage of 30 kV with intermediate polishing steps at 5 and 2 kV. Samples for transmission electron microscopy (TEM) were prepared on the same tool and imaged, after plasma cleaning, on a JEOL JEM 2200 FS operated at 200 kV. A Bruker D8 in θ−2θ configuration was used for X-ray diffraction (XRD) at grazing incidence in out-of-plane (1°) and in-plane (1.5°) geometry using Cu Kα radiation (wavelength 1.5425 Å).

Time-of-flight secondary ion mass spectrometry (TOF-SIMS) was performed on an ION-TOF with a 25 keV Bi^+ primary ion beam for recording mass spectra and a 2 keV O_2^+ ion beam for depth profiling at a sputter rate of 0.5 nm/s. An electron flood gun was used for charge compensation. TOF-SIMS spectra were calibrated using the data from elastic recoil detection analysis (ERDA) performed with 13 MeV $^{127}I^+$ beam at 18° incidence angle. Recoils scattered to 36° were identified by combining a TOF spectrometer with a gas ionization chamber.

EIS was performed using a Paios Fluxim impedance spectrometer in the frequency range of 10 mHz to 0.1 MHz with an amplitude of 50 mV. Temperature-dependent measurements were performed in steps of 10 °C using a Linkam LTSE-420-P heating stage in an argon atmosphere. The temperature was measured on the sample surface with a Pt100 thermocouple. The samples were contacted with 100 nm sputtered Pt electrodes prepared with a Leica EM ACE600 sputter coater.

RESULTS AND DISCUSSION

We first discuss the crystal structure of $Li_4Ti_5O_{12}$ reported in the literature and shown in Figure 1a. It is a cubic spinel with space group $Fd\bar{3}m$. The tetrahedral 8a sites are occupied by lithium (orange), the octahedral 16d sites by titanium (green) or lithium with occupancy ratio Ti/Li 5:1, and the 32e sites by oxygen (red).[1,14,15] The octahedral 16c sites are empty (dashed circle). The reported values for the lattice parameter of the spinel $Li_4Ti_5O_{12}$ are in the range of 8.352−8.367 Å.[1,7,14,16−18] Figure 1b shows the crystallographic structure after lithiation to $Li_7Ti_5O_{12}$. Here, the 16c sites are filled with lithium, whereas the 8a sites are now empty, as shown by Wagemaker et al. using neutron diffraction.[19] The 16d sites remain unaltered, and the structure can be described as rock-salt type ($Fm\bar{3}m$), with lattice parameter in the range of 8.352−8.368 Å.[14,18] The small change in the lattice parameter is one reason for the high stability of $Li_xTi_5O_{12}$ ($4 \leq x \leq 7$) for electrochemical cycling[1] but hinders the unambiguous distinction of the spinel and rock-salt phases by XRD.

Figure 1c,d shows the SEM images of the FIB cross sections of the epitaxial and polycrystalline $Li_4Ti_5O_{12}$ thin films, respectively, which were deposited in the same run. Both films are 125 nm thin, dense, and crack-free. A layer of Pt, visible in both images, was electron- and ion-beam deposited on top of both films to protect the sample from ion damage during FIB cutting. Moreover, top view SEM images in Figure S3 show that the polycrystalline film is composed of particles with a lateral size of a few tens of nanometers, whereas the epitaxial film appears uniform and flat. To nucleate and grow

DOI: 10.1021/acsami.8b16519
ACS Appl. Mater. Interfaces 2018, 10, 44494−44500

the epitaxial $Li_4Ti_5O_{12}$(111) thin film, we employed a single-crystal MgO(111) substrate, which has a lattice parameter of 4.214 Å[20] and therefore, considering its double lattice parameter, a lattice mismatch with $Li_4Ti_5O_{12}$ smaller than 1%. The polycrystalline $Li_4Ti_5O_{12}$ thin film was deposited on a ~70 nm thick polycrystalline MgO film on the Si(100) wafer,[21] which acts as a buffer layer for the nucleation and growth of polycrystalline $Li_4Ti_5O_{12}$. To grow polycrystalline MgO, the Si(100) wafer was employed as substrate because Si(100) is not lattice-matched with MgO(100) or MgO(111). Sputtering of MgO onto MgO(111) substrate resulted in the oriented growth of MgO. To avoid lithium deficiency in the films caused by scattering of lithium in the ablation plume and sublimation of lithium once deposited on the substrate,[22,23] we employed high laser fluence (2.6 J/cm^2) and lithium-enriched ablation targets ($Li_{5.35}Ti_5O_{12}$).

To quantitatively determine the lithium content in $Li_xTi_5O_{12}$ across the film thickness, we performed TOF-SIMS profiling and used ERDA to calibrate the lithium signal. The resulting profiles for the epitaxial and polycrystalline films are reported in Figure 1e. The interface between the films and the substrates is set at 0 nm depth. Maximum $^{24}Mg^+$ and $^{28}Si^+$ intensities are normalized to 1. Because the $^7Li^+$ signal saturated the detector even at low Bi^+ ion beam current, the $^6Li^+$ signal is reported. Both films have a stoichiometry of $x = 4$, expected for the spinel phase $Li_4Ti_5O_{12}$, and the $^6Li^+$ signal is constant across the film thickness, showing a uniform lithium content. For both films, the $^6Li^+$ signal decreases sharply with the concurrent increase of the $^{24}Mg^+$ signal, indicating a relatively sharp interface. Interestingly, the $^6Li^+$ signal of the polycrystalline film shows a small but well-defined peak near 100 nm depth. This can be explained by imperfections in the MgO layer through which Li could alloy with Si.[21]

Figure 2a,b shows the TEM images of epitaxial and polycrystalline $Li_4Ti_5O_{12}$, respectively. The fast Fourier transforms (FFTs) of the highlighted regions are reported as insets. To demonstrate the epitaxial growth of $Li_4Ti_5O_{12}$ on MgO(111), a TEM lamella of the FIB cross section was imaged along the $[11\text{-}2]_{MgO}$ zone axis orientation and is reported in Figure 2a. The interface between the film and the substrate is coherent, and the film has high crystalline quality. Moreover, the reported FFTs show that the film is oriented, lattice-matched with the substrate, and grows strain free. Figure 2b shows an exemplary high-resolution image of the polycrystalline film grain structure. The selected grain is 9.2 ± 1.4 nm wide and longer than 25 nm and represents an average found for the nanostructure. The FFTs of the selected areas show different diffraction spots, indicating that the grains have different crystallographic orientation. Moreover, close inspection of the polycrystalline film shows amorphous parts, which could extend the grain boundary region.

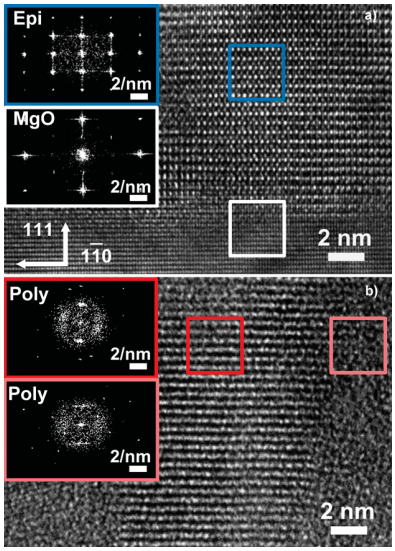

Figure 2. TEM images of (a) epitaxial $Li_4Ti_5O_{12}$ along the [11-2] direction and (b) polycrystalline $Li_4Ti_5O_{12}$. The FFTs of the highlighted regions of the films and substrates are reported as insets.

To further prove epitaxy and characterize the polycrystalline film, we use XRD as shown in Figure 3. Figure 3a shows the out-of-plane and the grazing-incidence XRD data for the epitaxial and polycrystalline films, respectively. The epitaxial film shows a reflection at $2\theta = 18.357°$, which corresponds to the (111) $Li_4Ti_5O_{12}$ reflection, and additional reflections at 36.97 and 78.84°, which correspond to the (111) and (222) MgO substrate reflections, respectively. The lattice parameter calculated from the (111) $Li_4Ti_5O_{12}$ reflection is 8.364 ± 0.001 Å, in agreement with the literature.[1] The full width at half-maximum (fwhm) of the (111) reflection is 0.163° and was calculated by performing a Lorentzian fit and subtracting the instrumental broadening of 0.103°. Using the Scherrer formula (shape factor $K = 1$),[24] the estimated coherent diffraction length is ~50 nm. Differently from the epitaxial film, the polycrystalline film shows many more reflections associated with $Li_4Ti_5O_{12}$. Here, the fwhm of the (111) reflection is 0.343°, from which we estimate an average out-of-plane grain size of ~25 nm. Interestingly, the (111) reflection shows higher intensity than the reference diffraction data,[17] indicating the (111) out-of-plane preferred orientation (texture). To quantify the degree of texture, we performed Rietveld refinement of the diffractogram and employed the March−Dollase approach,[25,26] in which a probability distribution function depending on the parameter r corrects for the texture in the film. When the crystallites are randomly oriented, r is equal to 1, whereas when the crystallites are uniaxially oriented, r is equal to 0. Here, the obtained March−Dollase parameter r is 0.33, therefore indicating a strong (111) out-of-plane texture.

We now focus on the in-plane X-ray diffractograms, reported in Figure 3b. To investigate the in-plane orientation of the epitaxial and polycrystalline films, the X-ray source was set at a grazing angle of 1.5° and a coupled in-plane $\theta-2\theta$ scan was performed (see inset in Figure 3b). The epitaxial film has one reflection at 63.81° with a shoulder at lower angles (62.74°), which correspond to the substrate MgO (2-20) and $Li_4Ti_5O_{12}$ (4-40) reflections, respectively. The diffractogram shows that the film and the substrate are lattice-matched and aligned along the [1-10] direction. These results are in agreement with the TEM data and confirm the epitaxial growth of $Li_4Ti_5O_{12}$ on MgO. In the in-plane diffractogram of the polycrystalline film, the main $Li_4Ti_5O_{12}$ reflections are visible. The (4-40) reflection exhibits an uncharacteristically high intensity. Because the (4-40) crystallographic planes are perpendicular to (111), this high intensity confirms that the film is strongly textured in agreement with the analysis of the out-of-plane diffractogram. From the fwhm of the (4-40) reflection, we estimate an average in-plane grain size lower than 10 nm, which is of the

DOI: 10.1021/acsami.8b16519
ACS Appl. Mater. Interfaces 2018, 10, 44494−44500

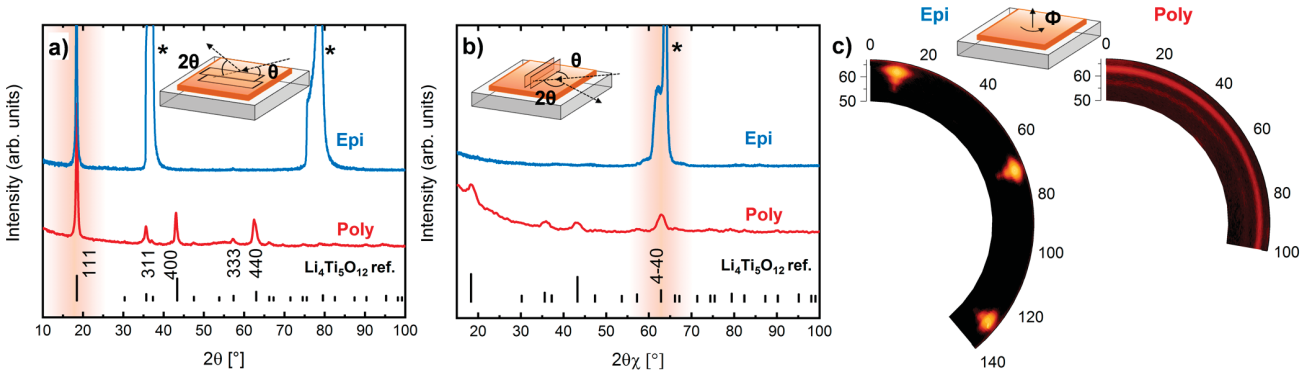

Figure 3. (a) Out-of-plane, grazing incidence, and (b) in-plane XRD of epitaxial and polycrystalline $Li_4Ti_5O_{12}$ films. (c) In-plane pole figure of epitaxial (f = 0−120°) and polycrystalline $Li_4Ti_5O_{12}$ films (f = 0−100°). Sketches of the corresponding measurement geometry are drawn as an inset.

same order of magnitude as the lateral size of the exemplary grain observed in TEM in Figure 2b.

We now discuss the in-plane orientation of the films in Figure 3c. Here, the in-plane θ−2θ diffractograms are recorded for every ϕ from 0 to 140° and from 0 to 100° (ϕ step size of 1°) for the epitaxial and polycrystalline film, respectively. The pole figure of the epitaxial film shows three discrete reflections equally spaced 60° apart from each other, consistent with the sixfold azimuthal symmetry of the (111) surface, confirming the epitaxial growth. The pole figure of the polycrystalline film shows continuous rings instead, indicating that the grains are randomly oriented in the azimuthal direction.

To investigate the Li-ion conductivity of the epitaxial and polycrystalline $Li_4Ti_5O_{12}$ thin films, we performed EIS. Spectra were recorded in the frequency range of 0.01−10^5 Hz in steps of 10 °C from 200 to 350 °C using a heating rate of 0.1 °C/s in an argon atmosphere. The contacts were fabricated by depositing 3.2 × 0.5 mm^2 Pt pads with a thickness of 100 nm by dc sputtering. The electrodes were 190 μm apart (in-plane configuration), and the sample was contacted using Au-coated tungsten microprobes (see inset in Figure 4a). The geometric factor $F = 2.10 \times 10^{-6}$ m was calculated by dividing the active electrode area by the distance between the electrodes. In the in-plane measurement geometry, the active electrode area is calculated by multiplying the electrode length by the film thickness, which is a good approximation for thin films (with negligible voltage drop in the direction perpendicular to the plane).

Figure 4a shows examples of Nyquist plots for the epitaxial and polycrystalline films measured at 230 °C (see Figure S1 for data at other temperatures). In a Nyquist plot, each data point represents the complex impedance at a single frequency, which increases from the right to the left in the plot. The impedance data of the epitaxial film take the shape of a perfect semicircle. Consequently, it can be fitted with an RC equivalent circuit, where the resistor R and the capacitor C are in parallel. The impedance takes the form $Z_{RC}(\omega) = (R^{-1} + i\omega C)^{-1}$, where ω is the angular frequency. Because $Li_4Ti_5O_{12}$ is electronically insulating with reported room temperature values for the electronic conductivity of 10^{-7}−10^{-8} S/cm,[27] R corresponds to the resistance to Li-ion transport. An even lower value for an electronic conductivity of <10^{-13} S/cm was reported by Chen et al.[28] and is often cited in the literature,[3,29] but the authors point out that the exact value "could not be determined accurately within the resolution of the multimeter". The

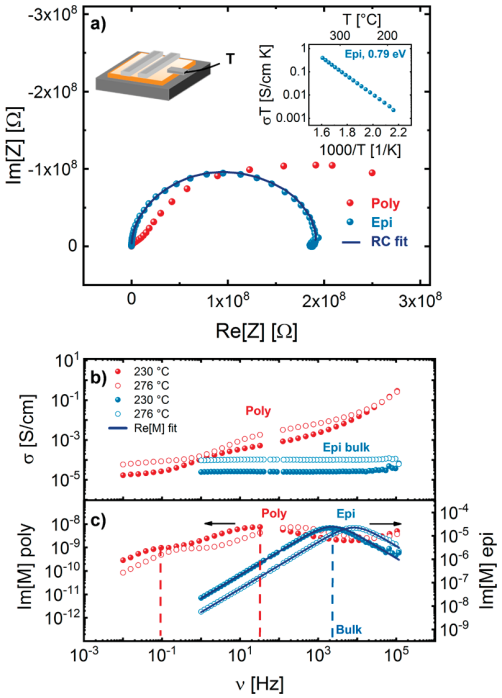

Figure 4. (a) Nyquist plot of epitaxial and polycrystalline $Li_4Ti_5O_{12}$. The measurement geometry and the Arrhenius plot of the epitaxial film are reported as inset. (b) Examples of conductivity and (c) electric modulus vs frequency plots for epitaxial and polycrystalline $Li_4Ti_5O_{12}$ measured at 230 and 276 °C.

resistance can then be extracted from the low-frequency intersection of the semicircle with the horizontal axis in the Nyquist plot of the impedance. The ionic conductivity obtained as $1/R \times F$ is 2.5×10^{-5} S/cm at 230 °C, at least two orders of magnitude higher than the electronic conductivity of the material. As a function of temperature, the Li-ion conductivity shows a typical Arrhenius behavior, with an activation energy of 0.79 eV (see inset in Figure 4a). At high temperatures and low frequencies, the onset of electrode polarization becomes visible for the epitaxial film (see inset of Figure S1a). The conductivity at 230 and 276 °C as a function of frequency is plotted in Figure 4a and was calculated from the complex impedance via $\sigma(\omega) = \mathrm{Re}[Z(\omega)]/F(\mathrm{Re}[Z(\omega)]^2 + \mathrm{Im}[Z(\omega)]^2)$. Data points that lie on a perfect semicircle in the Nyquist plot take a constant value of $1/R \times F$ in this plot,

DOI: 10.1021/acsami.8b16519
ACS Appl. Mater. Interfaces 2018, 10, 44494−44500

representing again the frequency-independent dc conductivity of the system.

Yet another representation of the data, useful for the following discussion of the polycrystalline film, is shown in Figure 4c. Here, we plot the imaginary part of the electric modulus related to the complex impedance via $M(\omega) = i\omega F\varepsilon_0 Z(\omega)$,[30,31] where ε_0 is the vacuum permittivity (8.854×10^{-12} F/m). For the parallel RC circuit, $\mathrm{Im}[M(\omega)]$ takes the form $\omega F\varepsilon_0 R/(\omega^2 C^2 R^2 + 1)$. This function reaches a maximum at the characteristic frequency $1/RC$. For frequencies lower than $1/RC$, $\mathrm{Im}[M(\omega)]$ is proportional to ω, thus exhibiting a linear behavior in a log−log plot with a slope of 1. At frequencies higher than $1/RC$, $\mathrm{Im}[M(\omega)]$ is proportional to ω^{-1}, thus exhibiting a slope of −1 in the log−log plot consistent with the data shown in Figure 4c. Thus, the data of the epitaxial film can be modeled consistently with a simple equivalent parallel RC circuit.

The case is more complex for the polycrystalline film. In the Nyquist plot in Figure 4a, we can no longer discern a clear semicircle. The common approach is to fit the data in the Nyquist plot with several semicircles representing processes taking place at different characteristic time scales RC. For polycrystalline samples, often two semicircles with two different RC values are chosen to represent bulk and grain boundary processes.[13] However, the low-frequency part of the Nyquist plot of the polycrystalline film exhibits a strongly depressed incomplete semicircular shape, which cannot be modeled by a simple parallel RC circuit. Depressed semicircles are often modeled using a resistor R in parallel with a constant phase element (CPE), representing a nonideal capacitor and having a controversial physical meaning.[32] The impedance then takes the form $Z_{\text{R-CPE}}(\omega) = R[1 + R(i\omega RC)^n]^{-1}$, adding an additional parameter n, which governs the degree of depression of the semicircle, with $n = 1$ representing the case of the ideal parallel RC circuit (see Figure S2). For the polycrystalline film, this extension of the model does not constitute an improvement. The determination of the dc conductivity would require extrapolation of this depressed semicircle to lower frequency, which is delicate because of the three independent parameters (or six parameters if two depressed semicircles are considered).

Also from the conductivity versus frequency plot in Figure 4b, a straightforward extraction of the dc conductivity is not possible, as the conductivity does not reach a constant value even when extending the measurement window to frequencies as low as 0.01 Hz and increasing the temperature (see again Figure S1). It should also be emphasized that the geometric factor F may take different values for the different $1/RC$ processes, adding additional complexity to the data analysis.

The electric modulus representation in Figure 4c offers the advantage that the contributions from the individual processes can be distinguished more clearly. The electric modulus of the polycrystalline film shows two distinct maximums occurring at the two different characteristic frequencies $1/RC$. The frequencies at which the maximums occur are two (10 Hz) and four (0.1 Hz) orders of magnitude below the $1/RC$ frequency of the epitaxial film (10^3 Hz). This indicates that the processes in the two films occur at very different time scales, possibly resulting from the small grain size and extended grain boundary zone in the polycrystalline film. It is tempting to attribute these two processes to grain and grain boundary processes in the polycrystalline film. Some authors in the literature suggest that such behavior could rather be modeled by employing a particular distribution of relaxation times.[32] However, the slope on the low frequency side of the peaks in the electric modulus versus frequency log−log plot is smaller than 1 (in contrast to the epitaxial case), suggesting subdiffusive transport. A possible origin of this behavior is the trapping of Li ions due to structural disorder and/or polarization at grain boundaries.[32−34]

As expected, the value for the ionic dc conductivity of 2.5×10^{-5} S/cm at 230 °C extracted for the epitaxial model system is slightly higher than the values reported in the literature for polycrystalline pellets,[12,13] because of the absence of grain boundaries, porosity, and impurity phases. In particular, porosity and nonconducting impurity phases can lead to a significant reduction of the apparent ionic dc conductivity. For example, Wilkening et al. prepared polycrystalline pellets with an average grain size of 0.5 μm and observed an Arrhenius behavior with an activation energy of 0.94 eV and a conductivity of 4×10^{-6} S/cm at 238 °C.[12] In the measured frequency range (5 Hz−13 MHz) and temperature range (160−250 °C), the conductivity plot shows one plateau, which corresponds to one RC process.

On the contrary, Fehr et al.,[13] measuring polycrystalline pellets with an average grain size in the range of 0.8−1.5 and 0.1−0.3 μm, observed two stretched semicircles in the Nyquist plot, which they attributed to bulk and grain boundary processes and which they fitted with a parallel R-CPE circuit. Interestingly, they observed two distinct Arrhenius regimes, with activation energies in the range of 0.60 eV below ∼230 °C and higher than 0.80 eV above ∼470 °C, with a transition regime in between, which could suggest a phase change. At 230 °C, the estimated bulk conductivities are in the range of 3×10^{-6}−10^{-5} S/cm, consistent with Wilkening et al. It has also been shown by Iwaniak et al. that differently prepared samples can lead to differences in long-range dynamics possibly due to variations in defect density, microstructure, porosity, and so forth.[35]

The activation energy of the epitaxial film determined by EIS (probing macroscopic ion dynamics) is in excellent agreement with Li spin-lock nuclear magnetic resonance (NMR) and Li spin-alignment echo NMR, which sense long-range ion transport. For example, Wilkening et al. measured activation energies of 0.76 and 0.86 eV using these two methods, respectively.[12,36] The suggested hopping mechanism involves Li-vacancy trapping at the 16d sites.[15,37] On the contrary, spin−lattice relaxation NMR, which probes shorter length scales, showed activation energies of 0.26 and 0.35 eV.[12,15] Here, forward and backward hopping between 8a and vacant 16c sites has been the proposed mechanism, consistent with the calculation by Ziebarth et al.[37] Further experiments, including theoretical modeling, are required to understand and quantify the characteristics and impact of grain boundaries with the ultimate goal of controlling lithium ion transport across grain boundaries.

■ CONCLUSIONS

In conclusion, we studied the Li-ion conductivity of the battery material $Li_4Ti_5O_{12}$, which is a promising anode for all-solid-state batteries and microbatteries because of its low volume change upon lithium insertion. We demonstrate that unstrained phase-pure epitaxial $Li_4Ti_5O_{12}$ films (without grain boundaries) behave like an ideal ion conductor that can be modeled by single and parallel RC equivalent circuits. They possess an activation energy of 0.79 eV and a Li-ion

DOI: 10.1021/acsami.8b16519
ACS Appl. Mater. Interfaces 2018, 10, 44494−44500

conductivity of 2.5 × 10^{-5} S/cm at 230 °C, which can be extracted by fitting either a perfect semicircle to the Nyquist plot, extracting the value of the dc plateau from the conductivity versus frequency plot, or alternatively by fitting the electric modulus. The determination of the intrinsic conductivity of $Li_4Ti_5O_{12}$ was made possible by the utilization of epitaxial thin films. In contrast, the comparison of epitaxially grown $Li_4Ti_5O_{12}$ films to polycrystalline film with an average grain size of <10 nm and enlarged amorphous grain boundary area reveals the contributions to the impedance from several processes, which may be assigned to bulk and grain boundary, but no reliable dc conductivity can be extracted.

Meanwhile, our results are representative for the dramatic effect of grain boundaries on the lithium transport in $Li_4Ti_5O_{12}$ thin films; further experiments coupled with theoretical modeling are necessary to develop a detailed understanding of charge depletion/accumulation at grain boundaries and its effect on ion transport.[38] Importantly, designing MgO substrates with different surface morphologies is a possible strategy to control $Li_4Ti_5O_{12}$ thin film structural and transport properties. Ultimately, through this study, we demonstrate that epitaxial $Li_4Ti_5O_{12}$ can be grown on MgO substrates, providing alternative zero-strain anodes for future microbattery designs.

■ ASSOCIATED CONTENT

Supporting Information

The Supporting Information is available free of charge on the ACS Publications website at DOI: 10.1021/acsami.8b16519.

Nyquist, conductivity, and electric modulus plots for the epitaxial and polycrystalline films as a function of temperature. Simulated Nyquist, conductivity, and electric modulus plots for R-CPE parallel circuit at different *n* values (PDF)

■ AUTHOR INFORMATION

Corresponding Author

*E-mail: corsin.battaglia@empa.ch.

ORCID

Arndt Remhof: 0000-0002-8394-9646

Jennifer L. M. Rupp: 0000-0001-7160-0108

Corsin Battaglia: 0000-0002-5003-1134

Present Address

†ABB Corporate Research Ltd., CH-5405, Baden-Dättwil, Switzerland.

Notes

The authors declare no competing financial interest.

■ ACKNOWLEDGMENTS

We thank Léo Duchêne and Meike Heinz for valuable discussion. We thank the Nanoscale Materials Science laboratory at Empa for the TOF-SIMS access. This work was partially supported by the InnoSuisse through funding for the Swiss Competence Center for Energy Research (SCCER) Heat and Electricity Storage under contract number 1155-002545. J.L.M.R. thanks the Thomas Lord Foundation for financial support at MIT.

■ REFERENCES

(1) Colbow, K. M.; Dahn, J. R.; Haering, R. R. Structure and Electrochemistry of the Spinel Oxides $LiTi_2O_4$ and $Li_{4/3}Ti_{5/3}O_4$. *J. Power Sources* **1989**, *26*, 397−402.

(2) Haetge, J.; Hartmann, P.; Brezesinski, K.; Janek, J.; Brezesinski, T. Ordered Large-Pore Mesoporous $Li_4Ti_5O_{12}$ Spinel Thin Film Electrodes with Nanocrystalline Framework for High Rate Rechargeable Lithium Batteries: Relationships among Charge Storage, Electrical Conductivity and Nanoscale Structure. *Chem. Mater.* **2011**, *23*, 4384−4393.

(3) Chen, S.; Xin, Y.; Zhou, Y.; Ma, Y.; Zhou, H.; Qi, L. Self-Supported $Li_4Ti_5O_{12}$ Nanosheet Arrays for Lithium Ion Batteries with Excellent Rate Capability and Ultralong Cycle Life. *Energy Environ. Sci.* **2014**, *7*, 1924.

(4) Kato, Y.; Hori, S.; Saito, T.; Suzuki, K.; Hirayama, M.; Mitsui, A.; Yonemura, M.; Iba, H.; Kanno, R. High-Power All-Solid-State Batteries Using Sulfide Superionic Conductors. *Nat. Energy* **2016**, *1*, 16030.

(5) Deng, J.; Lu, Z.; Belharouak, I.; Amine, K.; Chung, C. Y. Preparation and Electrochemical Properties of $Li_4Ti_5O_{12}$ Thin Film Electrodes by Pulsed Laser Deposition. *J. Power Sources* **2009**, *193*, 816−821.

(6) Mosa, J.; Vélez, J. F.; Lorite, I.; Arconada, N.; Aparicio, M. Film-Shaped Sol−Gel $Li_4Ti_5O_{12}$ Electrode for Lithium−Ion Microbatteries. *J. Power Sources* **2012**, *205*, 491−494.

(7) Verde, M. G.; Baggetto, L.; Balke, N.; Veith, G. M.; Seo, J. K.; Wang, Z.; Meng, Y. S. Elucidating the Phase Transformation of $Li_4Ti_5O_{12}$ Lithiation at the Nanoscale. *ACS Nano* **2016**, *10*, 4312−4321.

(8) Hirayama, M.; Kim, K.; Toujigamori, T.; Cho, W.; Kanno, R. Epitaxial Growth and Electrochemical Properties of $Li_4Ti_5O_{12}$ Thin-Film Lithium Battery Anodes. *Dalton Trans.* **2011**, *40*, 2882−2887.

(9) Hirayama, M.; Shibusawa, T.; Yamaguchi, R.; Kim, K.; Taminato, S.; Yamada, N. L.; Yonemura, M.; Suzuki, K.; Kanno, R. Neutron Reflectometry Analysis of $Li_4Ti_5O_{12}$/Organic Electrolyte Interfaces: Characterization of Surface Structure Changes and Lithium Intercalation Properties. *J. Mater. Res.* **2016**, *31*, 3142−3150.

(10) Pfenninger, R.; Afyon, S.; Garbayo, I.; Struzik, M.; Rupp, J. L. M. Lithium Titanate Anode Thin Films for Li-Ion Solid State Battery Based on Garnets. *Adv. Funct. Mater.* **2018**, *28*, 1800879.

(11) Hayashi, S.; Hatano, H. Ionic Conduction of $Li_2Ti_3O_7$ and $Li_4Ti_5O_{12}$. *J. Ceram. Soc. Jpn.* **1994**, 378−383.

(12) Wilkening, M.; Amade, R.; Iwaniak, W.; Heitjans, P. Ultraslow Li Diffusion in Spinel-Type Structured $Li_4Ti_5O_{12}$−A Comparison of Results from Solid State NMR and Impedance Spectroscopy. *Phys. Chem. Chem. Phys.* **2007**, *9*, 1239.

(13) Fehr, K. T.; Holzapfel, M.; Laumann, A.; Schmidbauer, E. DC and AC Conductivity of $Li_{4/3}Ti_{5/3}O_4$ Spinel. *Solid State Ionics* **2010**, *181*, 1111−1118.

(14) Murphy, D. W.; Cava, R. J.; Zahurak, S. M.; Santoro, A. Ternary Li_xTiO_2 Phases from Insertion Reactions. *Solid State Ionics* **1983**, *9*−*10*, 413−417.

(15) Schmidt, W.; Bottke, P.; Sternad, M.; Gollob, P.; Hennige, V.; Wilkening, M. Small Change—Great Effect: Steep Increase of Li Ion Dynamics in $Li_4Ti_5O_{12}$ at the Early Stages of Chemical Li Insertion. *Chem. Mater.* **2015**, *27*, 1740−1750.

(16) Ariyoshi, K.; Yamato, R.; Ohzuku, T. Zero-Strain Insertion Mechanism of $Li[Li_{1/3}Ti_{5/3}]O_4$ for Advanced Lithium-Ion (Shuttlecock) Batteries. *Electrochim. Acta* **2005**, *51*, 1125−1129.

(17) Kataoka, K.; Takahashi, Y.; Kijima, N.; Akimoto, J.; Ohshima, K.-I. Single Crystal Growth and Structure Refinement of $Li_4Ti_5O_{12}$. *J. Phys. Chem. Solids* **2008**, *69*, 1454−1456.

(18) Scharner, S.; Weppner, W.; Schimid-Beuermann, P. Evidence of Two-Phase Formation upon Lithium Insertion into the $Li_{1.33}Ti_{1.67}O_4$ Spinel. *J. Electrochem. Soc.* **1999**, *146*, 857−861.

(19) Wagemaker, M.; Simon, D. R.; Kelder, E. M.; Schoonman, J.; Ringpfeil, C.; Haake, U.; Lützenkirchen-Hecht, D.; Frahm, R.; Mulder, F. M. A Kinetic Two-Phase and Equilibrium Solid Solution in Spinel $Li_{4+x}Ti_5O_{12}$. *Adv. Mater.* **2006**, *18*, 3169−3173.

(20) Tsirelson, V. G.; Avilov, A. S.; Abramov, Y. A.; Belokoneva, E. L.; Kitaneh, R.; Feil, D. X-ray and Electron Diffraction Study of MgO. *Acta Crystallogr., Sect. B: Struct. Sci., Cryst. Eng. Mater.* **1998**, *54*, 8−17.

(21) Wen, C. J.; Huggins, R. A. Chemical Diffusion in Intermediate Phases in the Lithium-Silicon System. *J. Solid State Chem.* **1981**, *37*, 271−278.
(22) Packwood, D. M.; Shiraki, S.; Hitosugi, T. Effects of Atomic Collisions on the Stoichiometry of Thin Films Prepared by Pulsed Laser Deposition. *Phys. Rev. Lett.* **2013**, *111*, 036101.
(23) Hitosugi, T.; Packwood, D.; Shiraki, S. Atomic Collision Effects during PLD Processes: Nonstoichiometry Control in Transparent Superconductors. In *Proceedings Oxide-Based Materials and Devices*, SPIE OPTO, San Francisco, CA, February 1−6, 2014; SPIE: Bellingham, WA, 2014; 89870U, DOI: 10.1117/12.2045551.
(24) Scherrer, P. Bestimmung der Grosse und der Inneren Struktur von Kolloidteilchen Mittels Rontgenstrahlen. *Math.-Phys. Kl.* **1918**, *2*, 98−100.
(25) March, A. Mathematische Theorie der Regelung nach der Korngestalt bei Affiner Deformation. *Z. Kristallog.* **1932**, *81*, 285−297.
(26) Dollase, W. A. Correction of Intensities for Preferred Orientation in Powder Diffractometry: Application of the March Model. *J. Appl. Crystallogr.* **1986**, *19*, 267−272.
(27) Young, D.; Ransil, A.; Amin, R.; Li, Z.; Chiang, Y.-M. Electronic Conductivity in the $Li_{4/3}Ti_{5/3}O_4$−$Li_{7/3}Ti_{5/3}O_4$ System and Variation with State-of-Charge as a Li Battery Anode. *Adv. Energy Mater.* **2013**, *3*, 1125−1129.
(28) Chen, C. H.; Vaughey, J. T.; Jansen, A. N.; Dees, D. W.; Kahaian, A. J.; Goacher, T.; Thackeray, M. M. Studies of Mg-Substituted $Li_{4-x}Mg_xTi_5O_{12}$ Spinel Electrodes ($0 < x < 1$) for Lithium Batteries. *J. Electrochem. Soc.* **2001**, *148*, A102−A104.
(29) Yi, T.-F.; Yang, S.-Y.; Xie, Y. Recent Advances of $Li_4Ti_5O_{12}$ as a Promising next Generation Anode Material for High Power Lithium-Ion Batteries. *J. Mater. Chem. A* **2015**, *3*, 5750−5777.
(30) Hodge, I. M.; Ngai, K. L.; Moynihan, C. T. Comments on the Electric Modulus Function. *J. Non.-Cryst. Solids* **2005**, *351*, 104−115.
(31) Habasaki, J.; Leon, C.; Ngai, K. L. *Dynamics of Glassy, Crystalline and Liquid Ionic Conductors*; Springer: Cham, Switzerland, 2017; Vol. *132*, DOI: 10.1007/978-3-319-42391-3.
(32) Barsoukov, E.; Macdonald, J. R., Eds. *Impedance Spectroscopy Theory, Experiment, and Applications*; John Wiley & Sons: Hoboken, NJ, 2005.
(33) Cuervo-Reyes, E.; Scheller, C. P.; Held, M.; Sennhauser, U. A Unifying View of the Constant-Phase-Element and Its Role as an Aging Indicator for Li-Ion Batteries. *J. Electrochem. Soc.* **2015**, *162*, A1585−A1591.
(34) Bisquert, J.; Compte, A. Theory of the Electrochemical Impedance of Anomalous Diffusion. *J. Electroanal. Chem.* **2001**, *499*, 112−120.
(35) Iwaniak, W.; Fritzsche, J.; Zukalová, M.; Winter, R.; Wilkening, M.; Heitjans, P. Li Conductivity of Nanocrystalline $Li_4Ti_5O_{12}$ Prepared by a Sol-Gel Method and High-Energy Ball Milling. *Defect Diffus. Forum* **2009**, *289−292*, 565−570.
(36) Wilkening, M.; Iwaniak, W.; Heine, J.; Epp, V.; Kleinert, A.; Behrens, M.; Nuspl, G.; Bensch, W.; Heitjans, P. Microscopic Li Self-Diffusion Parameters in the Lithiated Anode Material $Li_{4+x}Ti_5O_{12}$ ($0 \leq x \leq 3$) Measured by ^{7}Li Solid State NMR. *Phys. Chem. Chem. Phys.* **2007**, *9*, 6199−6202.
(37) Ziebarth, B.; Klinsmann, M.; Eckl, T.; Elsässer, C. Lithium Diffusion in the Spinel Phase $Li_4Ti_5O_{12}$ and in the Rocksalt Phase $Li_7Ti_5O_{12}$ of Lithium Titanate from First Principles. *Phys. Rev. B: Condens. Matter Mater. Phys.* **2014**, *89*, 174301.
(38) Braun, S.; Yada, C.; Latz, A. Thermodynamically Consistent Model for Space-Charge-Layer Formation in a Solid Electrolyte. *J. Phys. Chem. C* **2015**, *119*, 22281−22288.

DOI: 10.1021/acsami.8b16519
ACS Appl. Mater. Interfaces 2018, 10, 44494−44500